Friction **11**(11): 2073–2090 (2023)
https://doi.org/10.1007/s40544-022-0713-7
ISSN 2223-7690
CN 10-1237/TH
RESEARCH ARTICLE

Novel model of material removal rate on ultrasonic-assisted chemical mechanical polishing for sapphire

Mufang ZHOU, Min ZHONG, Wenhu XU*

Department of Mechanical Engineering, Key Laboratory of Tribology, Nanchang University, Nanchang 330031, China

Received: 30 August 2022 / Revised: 09 October 2022 / Accepted: 26 October 2022

© The author(s) 2022.

Abstract: Ultrasonic-assisted chemical mechanical polishing (UA-CMP) can greatly improve the sapphire material removal and surface quality, but its polishing mechanism is still unclear. This paper proposed a novel model of material removal rate (MRR) to explore the mechanism of sapphire UA-CMP. It contains two modes, namely two-body wear and abrasive-impact. Furthermore, the atomic force microscopy (AFM) *in-situ* study, computational fluid dynamics (CFD) simulation, and polishing experiments were conducted to verify the model and reveal the polishing mechanism. In the AFM *in-situ* studies, the tip scratched the reaction layer on the sapphire surface. The pit with a 0.22 nm depth is the evidence of two-body wear. The CFD simulation showed that abrasives could be driven by the ultrasonic vibration to impact the sapphire surface at high frequencies. The maximum total velocity and the air volume fraction (AVF) in the central area increased from 0.26 to 0.55 m/s and 20% to 49%, respectively, with the rising amplitudes of 1–3 μm. However, the maximum total velocity rose slightly from 0.33 to 0.42 m/s, and the AVF was nearly unchanged under 40–80 r/min. It indicated that the ultrasonic energy has great effects on the abrasive-impact mode. The UA-CMP experimental results exhibited that there was 63.7% improvement in MRR when the polishing velocities rose from 40 to 80 r/min. The roughness of the polished sapphire surface was R_a = 0.07 nm. It identified that the higher speed achieved greater MRR mainly through the two-body wear mode. This study is beneficial to further understanding the UA-CMP mechanism and promoting the development of UA-CMP technology.

Keywords: sapphire; ultrasonic-assisted chemical mechanical polishing (UA-CMP); material removal rate (MRR) predictive model; atomic force microscopy (AFM) *in-situ* studies; computational fluid dynamics (CFD)

1 Introduction

Sapphire is a transparent solid with high hardness, corrosion resistance, wear resistance, etc. [1, 2]. Therefore, sapphire materials are widely used in semiconductor lighting, chips, aerospace, and medical fields [3]. In all applications of sapphire, strict requirements on the surface morphology are set. Moreover, the chemical inertness and hard brittleness of sapphire also raise higher requirements for the surface polishing technique.

Chemical mechanical polishing (CMP) is a core technology in semiconductor manufacturing [4, 5]. It is popular and mature in sapphire polishing [6, 7]. CMP can produce an atomically smooth and undamaged surface [8–10]. However, traditional CMP usually employs toxic and polluted ingredients, leading to the pollution of environment. To overcome this challenge, Zhang et al. [11–14] have developed various new green slurries. These studies have reduced environmental pollution and significantly contributed to the improvement of CMP performance. Other scholars have also applied themselves to improve the sapphire CMP productivity and surface

* Corresponding author: Wenhu XU, flipreverse@126.com

profile. References [7, 15–20] have chosen to achieve better sapphire CMP effects by changing the size, material, and structure of the abrasive. References [21–23] have also been conducted to boost the CMP's performance by investigating factors such as the pH, catalyst, and dispersant of slurry. Parameters of the rotational speed, pressure, and time are investigated to guide the optimization of the sapphire polishing process in practical production [24–26]. Although the sapphire CMP has been continuously upgraded, the time cost is still high, and surface quality is hard to be improved [20, 27]. Thus, the development of new sapphire polishing techniques remains a priority.

In 1991 and 1992, Moriwaki et al. [28, 29] proposed the concept combining of ultrasonic vibration and ultra-precision machining techniques, which opened up new possibilities for the preparation of smooth surfaces [30–32]. Ultrasonic vibrations are well directed, causing the propagating mass to vibrate at high frequencies with large acceleration. At the same time, ultrasonic composite polishing has no dependence on the thermophysical action and electrical conductivity of the materials. This gives it a great advantage in processing stiff and fragile materials as sapphire [33–35]. After that, the sapphire ultrasonic-assisted chemical mechanical polishing (UA-CMP) system was reported [36, 37]. The material removal rate (MRR) of UA-CMP was twice as high as that of CMP. The surface roughness after UA-CMP was as low as 0.83 Å (root mean square (RMS)). Zhong et al. [38] found that compared with diamond and alumina, SiO_2 particles have the best polishing performance in sapphire ultrasonic polishing. Deng et al. [39] reported that 0.2% polyethylene glycol of slurry led to better results for UA-CMP. Sapphire UA-CMP has been proven to be feasible. However, the material removal mechanism has still not been fully revealed.

In order to clarify the CMP mechanism, Preston [40] firstly proposed an empirical equation for the material removal model. Su et al. [41] believed that solid–solid contact mode and hydro-dynamic mode coexist in silicon polishing under the condition of semi-contact lubrication. The two-body wear model of Luo and Dornfeld [42] took into account the plastic microcontact among the silicon wafer, abrasive particle, and pad. Chen et al. [43–47] adopted molecular dynamics theory to explore the abrasive-impact and novel three-body wear processes in silicon CMP. In the ultrasonic machining process, Zarepour and Yeo [48] developed an ultrasonic machining model based on the indentation fracture theory. The model considers that a single sharp abrasive particle removes the material by impacting the brittle silicon wafer. However, there are few MRR models available for sapphire polishing. The MRR model of sapphire UA-CMP that considers both two-body wear and abrasive-impact theory has not been reported. In this paper, the two-body wear and abrasive-impact material removal model of UA-CMP will be established by considering parameters such as the velocity, amplitude, and polishing load. Meanwhile, the two-body wear and abrasive-impact were investigated by the atomic force microscopy (AFM; Dimension edge, Bruker, USA) *in-situ* studies, computational fluid dynamics (CFD) simulations, and sapphire polishing experiments. It is meaningful to explore the sapphire UA-CMP mechanism and promote the development of UA-CMP technology.

2 Modeling

In this study, the pad material of UA-CMP is damping cloth. Abundant asperities and hollows can be found on the pad surface (Fig. 1(a)). The heights of asperities follow a normal distribution function. The pad surface roughness (S_a) is 24.8 μm. Figure 1(b) exhibits the scanning electron microscope (SEM; Phenom Star, Phenom-World, the Netherlands) morphology of abrasive particles, and they are spherical SiO_2 particles of approximately 60 nm. The workpiece is the sapphire wafer, which can be assumed to be a smooth plane compared to the pad surface.

During UA-CMP, the pad cannot completely touch sapphire due to the rough pad surface [49]. The gap between pad and sapphire will be filled with slurry. Therefore, the solid–solid and hydro-dynamic contact will coexist in UA-CMP, as shown in Fig. 2. In the solid–solid contact pattern, SiO_2 particles are inserted into the wafer–pad contact region, and form the two-body wear condition (Figs. 2(a) and 2(c)). Thus the reactive film on the sapphire surface is continuously

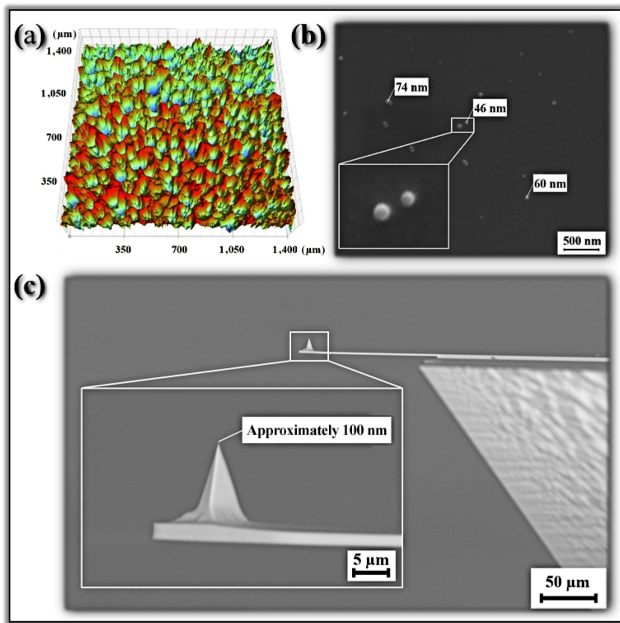

Fig. 1 Microstructures of pad, abrasive, and AFM tip: (a) three-dimensional (3D) topography of the pad surface; (b) SEM image of abrasive particles; and (c) SEM image of the AFM probe.

removed. The reactive layer is regarded as plastic deformation during the process. This material removal model is also the dominant idea in the current CMP contact model [50, 51]. The process can also be called as the ductile/plastic removal [52–54]. For the same reaction layer, brittle removal can be achieved when the indentation depth (l) of the abrasive exceeds the critical value. The critical indentation depth (l_c) can be solved as $l_c = \frac{0.15E}{H}\left(\frac{K}{H}\right)^2$ [54, 55], where K is the dynamic fracture toughness, and E and H are the elastic modulus and hardness, respectively.

In the hydro-dynamic contact mode, the slurry film in the wafer–pad gap flows continuously under the influences of the polishing speed and ultrasonic. Abrasives in the gap are named inactive abrasives [42]. The flowing slurry energizes inactive abrasives impacting/adhering to the reaction layer. The differences exist in sapphire UA-CMP and CMP. Some studies have pointed out the inactive abrasives in CMP contribute less to the MRR [42]. In UA-CMP, effects of ultrasonic energy enhance the role of inactive abrasives in MRR. Besides, ultrasonic vibration drives the inactive abrasives in the slurry to impact the reaction film at a high frequency and acceleration. The ultrasonic can also trigger cavitation, which can release transient local high temperature and pressure [56]. It accelerates the chemical reaction rate and increases the thickness of the reaction layer. The l of abrasive may exceed the critical condition because of the above factors. The abrasive-impact sparks the brittle removal of the material. Then, the reaction layer forms transverse and radial cracks, and the material will be removed, as depicted in Fig. 2(b). Liu et al. [57] immersed silicon wafers in the solution with SiO_2 particles, and the wafers were driven by ultrasonic. Significant pits are observed on the sample surface after the test. Reference [58] placed sapphire wafers into the silica slurry and applied ultrasonic vibration. Irregular pits were also found on the sapphire surface. The above researches prove that

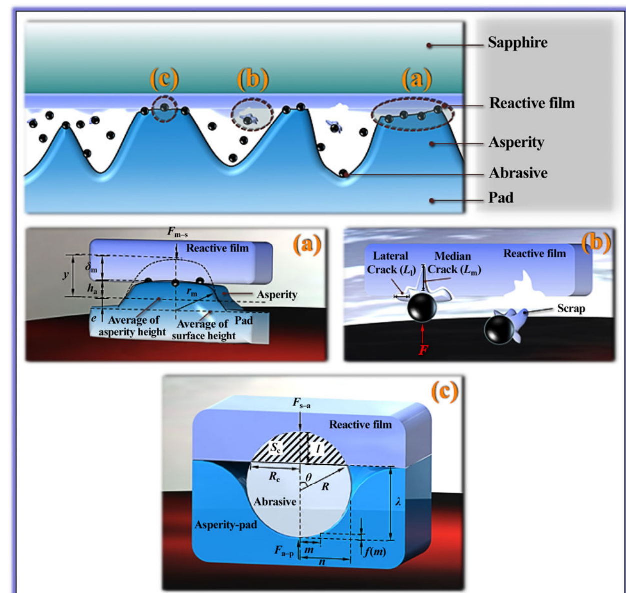

Fig. 2 Schematic diagram of the material removal principle of UA-CMP: (a) abrasives and pad asperity contact with reactive film in solid–solid contact pattern; (b) abrasive-impact model; and (c) two-body wear model of a single particle. Note: r_m represents the single asperity's radius, δ_m (= $y - h_a$, where y is the height of the asperity, and h_a indicates the distance from the asperities' mean height to sapphire) is its deformation, e is the difference between the average of asperity height and average of pad surface height, F_{m-s} is the interaction force, F_{s-a} is the force between the single particle and sapphire, l is the indentation depth, θ is half of the central angle about the diameter of the contact region between the single particle and reactive film, R_c is the radius of the contact region between the single particle and film, S_c is the cross-sectional area, R is the particle's radius, λ is the indentation, F_{a-p} is the contact force, n is the maximum contact radius of the particle and pad, m is the contact radius at a certain location within the contact profile, and $f(m)$ is the profile function of the abrasive particle embedded into the pad..

ultrasonic energy can achieve material removal by the mode of abrasive-impact (brittle removal).

2.1 Solid–solid contact mode

During UA-CMP, the wafer essentially contact with the asperities on the pad, so the real contact area (S_{real}) is less than that of the wafer surface. The contact region between an individual asperity and the wafer must be analyzed to calculate the S_{real}.

2.1.1 Contact analysis of pad and wafer

Figure 2(a) depicts a schematic diagram of the contact region between the single asperity and reactive film on the wafer surface. Based on Hertz contact theory [59], the contact area can be expressed as

$$S_{\text{m-s}} = \pi r_{\text{m}} \delta_{\text{m}} \tag{1}$$

where $S_{\text{m-s}}$ is the actual contact area between the single asperity and reaction film, r_{m} represents the single asperity's radius, and δ_{m} ($= y - h_{\text{a}}$, where y is the height of the asperity, and h_{a} indicates the distance from the asperities' mean height to sapphire) is its deformation.

The interaction force ($F_{\text{m-s}}$) between a single asperity and the wafer is

$$F_{\text{m-s}} = \frac{4}{3} E_{\text{s-p}} r_{\text{m}}^{1/2} \delta_{\text{m}}^{3/2} \tag{2}$$

where $E_{\text{s-p}}$ represents the composite elastic modulus of sapphire and pad, and can be given as

$$\frac{1}{E_{\text{s-p}}} = \frac{1-\upsilon_{\text{s}}^2}{E_{\text{s}}} + \frac{1-\upsilon_{\text{p}}^2}{E_{\text{p}}} \tag{3}$$

where υ_{p} and υ_{s} are the Poisson's ratios of the pad and wafer, respectively, and E_{s} and E_{p} are the elastic moduli of the sapphire and pad, respectively.

From the height distribution function of asperities on the pad, which can be expressed as $\varphi(y) = \frac{1}{\sqrt{2\pi}\sigma} \exp\left(-\left(\frac{y}{\sqrt{2}\sigma}\right)^2\right)$ [60] (σ is the pad's RMS roughness), and the number of asperities (N) in the nominal contact area is

$$N = \beta S_{\text{n}} \int_{h_{\text{a}}}^{+\infty} \varphi(y) \text{d}y \tag{4}$$

where β is the density of the pad, and S_{n} indicates the nominal contact zone of sapphire–pad. Therefore, the real contact region (S_{real}) can be written as

$$S_{\text{real}} = N \int_{h_{\text{a}}}^{+\infty} S_{\text{m-s}} \varphi(y) \text{d}y \tag{5}$$

Then, the real interaction force (F_{real}) and the S_{real} can be obtained according to Eqs. (1)–(5).

$$F_{\text{real}} = \frac{4}{3} \beta S_{\text{n}} E_{\text{s-p}} r_{\text{m}}^{1/2} \int_{h_{\text{a}}}^{+\infty} \delta_{\text{m}}^{3/2} \varphi(y) \text{d}y \tag{6}$$

$$S_{\text{real}} = \frac{3\pi r_{\text{m}}^{1/2} F_{\text{real}}}{4E_{\text{s-p}}} \frac{\int_{h_{\text{a}}}^{+\infty} \delta_{\text{m}} \varphi(y) \text{d}y}{\int_{h_{\text{a}}}^{+\infty} \delta_{\text{m}}^{3/2} \varphi(y) \text{d}y} \tag{7}$$

The integral term $\frac{\int_{h_{\text{a}}}^{+\infty} \delta_{\text{m}} \varphi(y) \text{d}y}{\int_{h_{\text{a}}}^{+\infty} \delta_{\text{m}}^{3/2} \varphi(y) \text{d}y}$ can be reduced to a constant C_{I} [61]. S_{real} and the real contact pressure (P_{real}) can be shown as

$$S_{\text{real}} = C_{\text{I}}^{-1} \left(\frac{h_{\text{a}}}{\sigma}\right)^{1/2} \frac{F_{\text{real}}}{E_{\text{s-p}}} \tag{8}$$

$$P_{\text{real}} = C_{\text{I}} \left(\frac{\sigma}{R}\right)^{1/2} E_{\text{s-p}} \tag{9}$$

where R is the particle's radius.

2.1.2 Analysis of contact between particle and wafer

During the sapphire UA-CMP using the SiO_2 slurry, Reactions (10)–(12) generally occur on the sapphire surface [16, 62–65].

$$Al_2O_3 + 2H_2O \rightarrow AlO(OH) + Al(OH)_3 \tag{10}$$

$$2SiO_2 + Al(OH)_3 + AlO(OH) \rightarrow Al_2Si_2O_7 \cdot 2H_2O \tag{11}$$

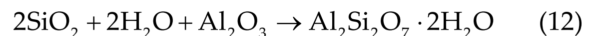

$$2SiO_2 + 2H_2O + Al_2O_3 \rightarrow Al_2Si_2O_7 \cdot 2H_2O \tag{12}$$

These reactions prove that the sapphire of high hardness (Mohs 9) will react to produce AlO(OH) (Mohs 3–4), $Al(OH)_3$ (Mohs 2.5–3.5), and $Al_2Si_2O_7 \cdot 2H_2O$ (Mohs 1.2–2) [66–69]. Under the action of load, SiO_2 particles (Mohs 7) tend to be pressed into the reactive film with lower hardness [67, 68, 70–72]. The process is considered as plastic deformation [73]. Figure 2(c) depicts the material removal mode as the two-body wear model. The l of abrasives in the

reactive film can be given by Eq. (13) [73]:

$$l = \frac{F_{s-a}}{2\pi HR} \quad (13)$$

where F_{s-a} is the force between the single particle and sapphire, and H is the hardness of the reactive film.

Meanwhile, the radius of the contact region between the single particle and film (R_c) can be expressed by Eq. (14):

$$R_c = \sqrt{R^2 - (R-l)^2} = \sqrt{R^2 - \left(R - \frac{F_{s-a}}{2\pi HR}\right)^2} \quad (14)$$

2.1.3 Analysis of contact between particle and pad

The pad is soft, and the load will likewise press the abrasive into it. According to the hyper-elastic contact theory, the indentation (λ) can be calculated by Eqs. (15) and (16) [74]:

$$\lambda = \int_0^1 \frac{f'(\chi)\mathrm{d}\chi}{\sqrt{1-\chi^2}} \quad (15)$$

$$2R = l + \lambda \quad (16)$$

where $\chi = \frac{m}{n}$, n is the maximum contact radius of the particle and pad, and m is the contact radius at a certain location within the contact profile. The contact force (F_{a-p}) can be obtained by Eq. (17):

$$F_{a-p} = 2E_{a-p} n \int_0^1 \frac{\chi^2 f(\chi)\mathrm{d}\chi}{\sqrt{1-\chi^2}} \quad (17)$$

where $\frac{1}{E_{a-p}}\left(=\frac{1-\upsilon_a^2}{E_a}+\frac{1-\upsilon_p^2}{E_p}\right)$ represents the composite elastic modulus considering abrasives and pads, υ_a and E_a are the particles' Poisson's ratio and elastic modulus, respectively, and its profile function of the abrasive particle embedded into the pad is $f(\chi) = R - \sqrt{R^2 - \chi^2 n^2}$ [74].

Hence,

$$\lambda = \frac{n}{2}\ln\left(\frac{R+n}{R-n}\right) \quad (18)$$

Since the condition of $\frac{n}{R} \le 1$ is satisfied, it can be derived by Taylor expansion.

$$\ln\left(\frac{R+n}{R-n}\right) \approx 2\left(\frac{n}{R} + \frac{n^3}{3R^3}\right) \quad (19)$$

Then,

$$\frac{F_{a-p}}{E_{a-p}R^2} = \frac{2\zeta + (\zeta-1)(\sqrt{9+12\zeta}-3)}{\sqrt{2}(\sqrt{9+12\zeta}-3)^{1/2}} \quad (20)$$

where $\zeta = \frac{\lambda}{R}$.

According to the force balance condition of the abrasive particle,

$$F_{a-p} = F_{s-a} \quad (21)$$

Equation (22) can be calculated as

$$\frac{H}{E_{a-p}} = \frac{2\zeta + (\zeta-1)(\sqrt{9+12\zeta}-3)}{2\sqrt{2}\pi(\sqrt{9+12\zeta}-3)^{1/2}} \quad (22)$$

It shows that ζ can be obtained from H and E_{a-p}. Besides,

$$R_c = R\sqrt{1-(\zeta-1)^2} \quad (23)$$

$$\theta = \arcsin(2-\zeta) \quad (24)$$

where θ is displayed in Fig. 2(c).

2.1.4 MRR model of two-body wear

The cross-sectional area (S_c) of the abrasive particle in the reaction layer is shown in Fig. 2(c). It can be expressed as

$$\begin{aligned} S_c &= \theta R^2 - R_c(R-l) \\ &= R^2\arcsin(2-\zeta) - R^2\sqrt{2\zeta-\zeta^2}(\zeta-1) \end{aligned} \quad (25)$$

The material removal volume (ΔU) by a single abrasive particle is

$$\Delta U = kS_c v_{p-s} t \quad (26)$$

where k is the wear coefficient, v_{p-s} represents the pad–wafer relative speed, and t is the polishing time.

The effective number of abrasives embedded in asperities can be given as

$$N_I = S_{real}\left(\frac{3\alpha}{4\pi R^3}\right)^{2/3} \quad (27)$$

where α is the abrasive volume concentration of the slurry.

Thus, the MRR model of two-body wear in sapphire UA-CMP can be represented as

$$\mathrm{MRR_{TBW}} = \frac{\Delta U N_{\mathrm{I}}}{S_{\mathrm{n}} t} = \left[\arcsin(2-\zeta) - \sqrt{2\zeta-\zeta^2}(\zeta-1)\right] \cdot \left(\frac{3}{4\pi}\right)^{2/3} C_{\mathrm{I}}^{-1} \left(\frac{R}{\sigma}\right)^{\frac{1}{2}} \frac{1}{E_{\mathrm{s-p}}} v_{\mathrm{p-s}} \alpha^{\frac{2}{3}} P_{\mathrm{n}} = C_{\mathrm{II}} \alpha^{2/3} P_{\mathrm{n}} v_{\mathrm{p-s}} \quad (28)$$

where P_{n} represents the nominal contact pressure, and $C_{\mathrm{II}} = \left[\arcsin(2-\zeta) - \sqrt{2\zeta-\zeta^2}(\zeta-1)\right]\left(\frac{3}{4\pi}\right)^{2/3} C_{\mathrm{I}}^{-1}\left(\frac{R}{\sigma}\right)^{1/2} \cdot \frac{1}{E_{\mathrm{s-p}}}$.

2.2 Hydro-dynamic contact mode

Hydro-dynamic contact is a mode, which uses the hydro-dynamic effects to process the wafer surface [41]. Under the influences of multiple potential energies, the multiple physical fields of the slurry will change significantly. Thus, the inactive abrasive particles in the slurry are able to impact/adhere to the chemical reaction layer, and achieve the material removal. Then, the MRR model can be established by the abrasive-impact theory.

In the UA-CMP process, ultrasonic vibration has strong effects on the flow behavior of the slurry. When the ultrasonic vibrates along the Z-axis, the Z-directional velocity (v_z), acceleration (a_z), and impact force (F_{ultra}) of the abrasive on the sapphire surface can be expressed as

$$v_z = wA\cos wt \quad (29)$$

$$a_z = -w^2 A\sin wt \quad (30)$$

$$F_{\mathrm{ultra}} = -w^2 mA\sin wt \quad (31)$$

where $w = 2\pi f$, and f and A are the frequency and amplitude of ultrasonic, respectively. The pressure of a single particle on the wafer (P_{ultra}) can be calculated as

$$P_{\mathrm{ultra}} = \frac{F_{\mathrm{ultra}}}{\pi R_{\mathrm{c}}^2} \quad (32)$$

According to the theory of indentation fracture, the impact of abrasives will cause lateral crack (L_{l}) and median crack (L_{m}) in the workpiece, as depicted in Fig. 2(b) [33, 75]. The dimensions of cracks can be obtained by Eqs. (33) and (34) [76, 77]

$$L_{\mathrm{l}} = G_{\mathrm{I}} \left(\frac{P_{\mathrm{ultra}}}{K_{\mathrm{Id}}}\right)^{\frac{3}{4}} \quad (33)$$

$$L_{\mathrm{m}} = G_{\mathrm{II}} \left(P_{\mathrm{ultra}} / H\right)^{\frac{1}{2}} \quad (34)$$

where G_{I} and G_{II} are scale factors, K_{Id} is the fracture toughness, and H is the hardness of the passivation layer. For a single abrasive particle, the volume of removed material in a vibration cycle can be derived as [77]

$$\Delta V_T = \frac{\pi}{3} L_{\mathrm{l}} L_{\mathrm{m}} \left|\overline{v_{\mathrm{p-w}}} + \overline{v_{\mathrm{ultra}}}\right| \frac{T}{2} = \frac{\pi}{3} L_{\mathrm{l}} L_{\mathrm{m}} \left[\frac{4\pi m f^2 A\sin 2\pi f t}{\zeta R^2 (2-\zeta) K_{\mathrm{Id}}}\right]^{\frac{3}{4}} \left[\frac{4\pi m f^2 A\sin 2\pi f t}{\zeta R^2 (2-\zeta) H}\right]^{\frac{1}{2}} \cdot \left|\overline{v_{\mathrm{p-w}}} + \overline{v_{\mathrm{ultra}}}\right| \frac{T}{2} \quad (35)$$

where T is the period of ultrasonic vibration, and $\overline{v_{\mathrm{p-w}}}$ and $\overline{v_{\mathrm{ultra}}}$ are the slurry velocity components in the XOY plane caused by the polishing speed and ultrasonic vibration, respectively.

The total material removal volume and MRR by the particle impact at the polishing time (T_1) can be written as

$$\Delta V_{T_1} = \frac{T_1}{T} \int_{T/2}^{T} N_{\mathrm{II}} \Delta V_T \mathrm{d}t \quad (36)$$

$$\mathrm{MRR_{AI}} = \frac{\Delta V_{T_1}}{S_{\mathrm{n}} T_1} = \frac{1}{T S_{\mathrm{n}}} \int_{T/2}^{T} N_{\mathrm{II}} \Delta V_T \mathrm{d}t \quad (37)$$

where $N_{\mathrm{II}} \left(= \frac{i\alpha V_{\mathrm{s}}}{V_{\mathrm{a}}} = \frac{3i\alpha}{4R}\left(h_{\mathrm{a}} + e + A\cos 2\pi f t\right)\right)$ [33] is the effective number of abrasive particles, i is the effective abrasive particle utilization, e is the difference between the average of asperity height and average of pad surface height, V_{s} is the volume of slurry in the contact area, and V_{a} is the volume of the individual abrasive particle.

By considering the effects of two-body wear, abrasive-impact, chemical action, cavitation, and other factors [74], the final $\mathrm{MRR_{all}}$ can be written as

$$\mathrm{MRR_{all}} = \kappa_1 \mathrm{MRR_{TBW}} + \kappa_2 \mathrm{MRR_{AI}} \quad (38)$$

where κ_1 and κ_2 are correction factors.

Throughout the two material removal models, they involve the influences of the process parameters including the polishing load, ultrasonic amplitude, and polishing speed. Subsequently, the AFM *in-situ* studies were applied to observe two-body wear processes. The CFD method was conducted to visualize the slurry behavior affecting the abrasive-impact because the slurry flow pattern is complex in UA-CMP. Polishing experiments were performed to evaluate the macro polishing effects.

3 AFM *in-situ* studies of two-body wear

To prove the feasibility of the two-body wear model, an *in-situ* study was carried out by the AFM. The difference in size and hardness between the AFM tip (Si) and the SiO_2 particle (Fig. 1) is not significant [62, 78, 79]. Therefore, it is feasible to simulate the chemical product removal process by controlling the tip to scratch the sapphire. It also enables the *in-situ* observation of the material removal process.

Before the *in-situ* study was performed, the sapphire roughness (R_a = 0.10 nm) was immersed in SiO_2 slurry for 24 h to generate the reaction layer. Figure 1(c) displays the SEM image of the AFM Si tip, and its size is approximately 100 nm. Then, *in-situ* studies of two-body wear were implemented in the liquid environment, which is ethanol with a 99.9% purity. It can prevent chemical reactions in the sapphire during *in-situ* studies [65]. The sapphire surface was scratched in the 1 μm × 1 μm range using the contact mode of the AFM, and the setpoint value is 7 V. The tapping mode of the AFM was used to image the original and scratched surfaces (6 μm × 6 μm), and the setpoint value is 2.8 V.

The results of the AFM *in-situ* study on two-body wear are given in Fig. 3. Comparing Figs. 3(a) and 3(c), the sapphire surface shows an obvious pit after the tip scribes the central area. Figure 3(b) shows the sapphire surface topography at 0 min. The atomic step structure is not completely exposed due to the presence of chemically reactive film [65]. The atomic step structure is prominent after 30 min of tip scratching due to the removal of the reaction layer. Its average thickness is about 0.22 nm (Fig. 3(d)), which is similar with the atomic step height (~0.22 nm) [65] on the sapphire surface. Hence, the atomic step structure is fuzzy on the sapphire surface at 0 min (Fig. 3(b)). However, few differences are found comparing the surface morphologies after 30 and 60 min processing (Fig. 3(b)). This indicates that the soft reaction layer has been completely removed, and the tip contacts the substrate, but it is hardly to damage the sapphire, which is much harder than the tip. Thus the surface morphology is basically unchanged. Figure 3(d) exhibits the height distribution profile of I–I cross-section in Fig. 3(c). Obviously, the touched region with the tip is significantly lower than the untouched region. The tip scribed the wafer surface

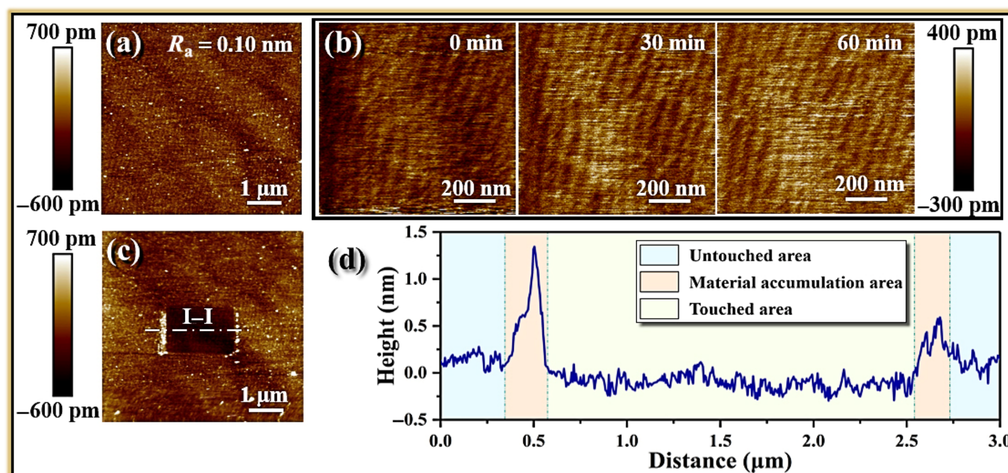

Fig. 3 Characterization of the AFM *in-situ* studies: (a) sapphire surface before scratching; (b) sapphire surface morphology changes during *in-situ* studies at different time; (c) sapphire surface after 60 min scratching; and (d) height distribution of I–I cross sectional profile.

in I–I direction, and the removed sapphire material from the contact area was accumulated on both the left and right sides (Figs. 3(c) and 3(d)). A similar phenomenon was also found in the study of Sheng et al. [80]. This *in-situ* study demonstrates the feasibility of the two-body wear in sapphire polishing.

4 Visualization of hydro-dynamic contact mode

This paper investigates the flow field variation patterns in UA-CMP by means of the CFD simulation methods. The aim is to test the feasibility of the hydro-dynamic contact mode and gain further insight into the UA-CMP mechanism. In the CFD simulation studies, the effects of ultrasonic amplitudes and polishing speeds on the slurry were studied. The pad's and wafer's speeds are the same in terms of values and direction. Table 1 exhibits the simulation schemes and parameters. The relevant parameter setup in the simulation model have been described in Ref. [58]. The UA-CMP process and location of the computational domain for the CFD simulations are depicted in Fig. 4.

Table 1 CFD simulation schemes and parameters of sapphire UA-CMP.

No.	Frequency (kHz)	Amplitude (μm)	Rotation speed (r/min)
1	50	1	60
2	50	2	60
3	50	3	60
4	50	2	40
5	50	2	80

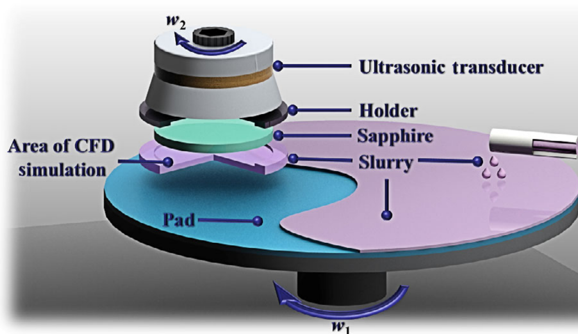

Fig. 4 Schematic diagram of the principle of UA-CMP and location of the CFD calculation domain. Note: w_1 is the angular velocity of the pad, and w_2 is the angular velocity of the sapphire wafer.

4.1 Effects of ultrasonic amplitudes on slurry fields

4.1.1 *Velocity field*

Figure 5 illustrates the total speed fields of the slurry on sapphire with 1 μm ultrasonic amplitude (A) along Z-axis. The black dotted circle shows the edge of the sapphire wafer. The contours indicate that the total velocity is distributed in a similar concentric trend at different time in one cycle. The total velocity at the edge location is greater than that in the central region. The crescent-shaped region of minimum velocity is located near the outlet. And the velocity distribution varies with time.

Figure 6 plots the total velocity distribution curves at the line segment of A–A (Fig. 5) under different amplitude conditions. It implies that higher ultrasonic amplitudes will result in greater velocities in the central region. Nevertheless, the fluid velocities at the edge have little change. Thus only fluid velocities in the central area were discussed and drew the following conclusions. At A = 1 μm, the maximum total velocity is approximately 0.26 m/s. As the amplitude increases to A = 2 and 3 μm, the maximum total velocity increases to roughly 0.37 and 0.55 m/s, respectively. Moreover, bigger ultrasonic amplitudes expand the variation range of total velocity within a single period, as presented in the insets of Fig. 6. The average total velocity of the slurry is enhanced, and the area of uniform distribution of total velocity is widened, displayed in the red rectangles. Therefore, the speeds of abrasive particles driven by the slurry rise and the shear abilities of the fluid and particle on the sapphire surface are strengthened. The hydro-dynamic contact pattern in UA-CMP is enhanced combining Eq. (35), which can get a higher MRR. In addition, the uniformity of sapphire polishing is also improved due to more uniform velocity distribution.

As demonstrated in Fig. 7(a), the distribution of v_z is nonuniform over the wafer surface with the ultrasonic vibration. In agreement with Eq. (29), higher values of ultrasonic amplitudes increase the peak of the slurry v_z, and v_z has a wider zone of uniform distribution, as shown in Figs. 7(a)–7(c). Comparing the three enlarged images (Figs. 7(a–a), 7(b–b), and 7(c–c)), the v_z difference among adjacent positions becomes larger owing to the higher amplitude. This potentially indicates a more complex flow behavior of

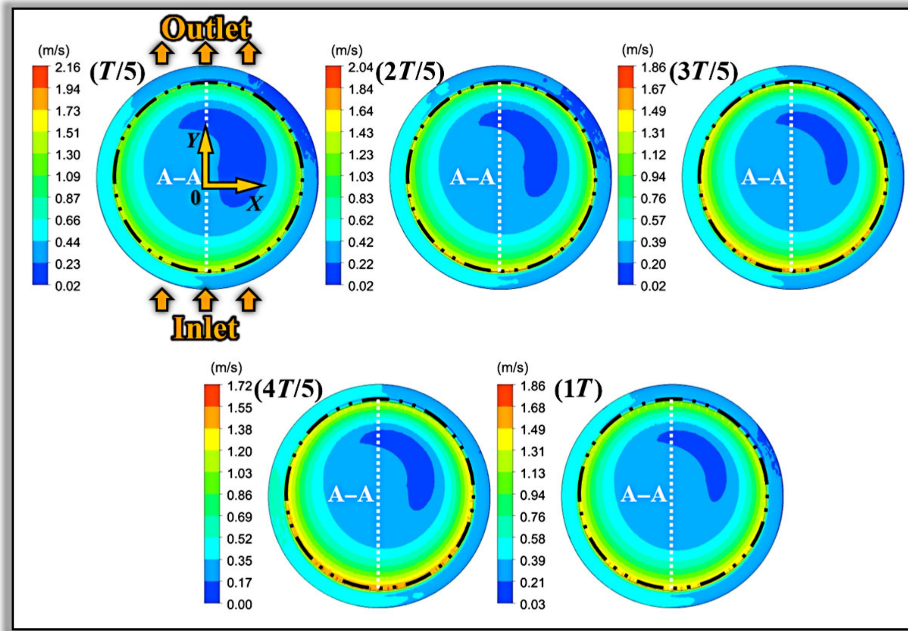

Fig. 5 Slurry velocity contours in one vibration period (T) with 1 μm amplitude, 50 kHz frequency, and 60 r/min rotating speed.

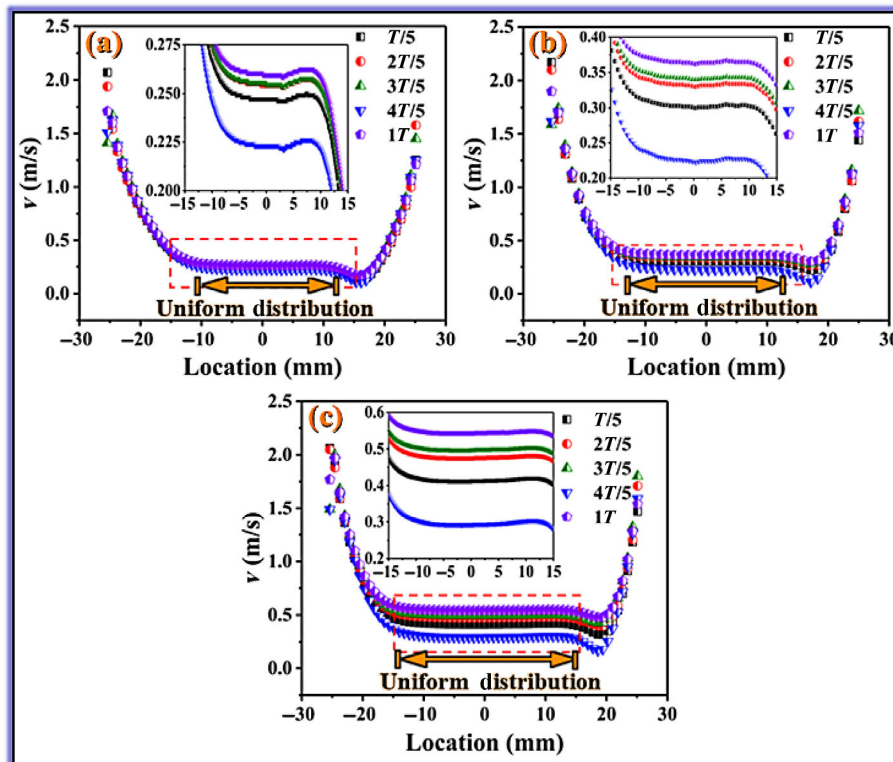

Fig. 6 Total velocity distribution curves of slurry under different amplitudes: (a) 1 μm; (b) 2 μm; and (c) 3 μm.

the fluid. Combined with Eqs. (29)–(34), the amplitude will affect the force, which is generated by the impact of particles on the sapphire surface. The force rises with the increasing amplitudes. It promotes the production of larger L_l and L_m. Meantime, more abrasives moving towards the wafer mean further gains in the abrasive utilization. This is a positive effect on the sapphire MRR.

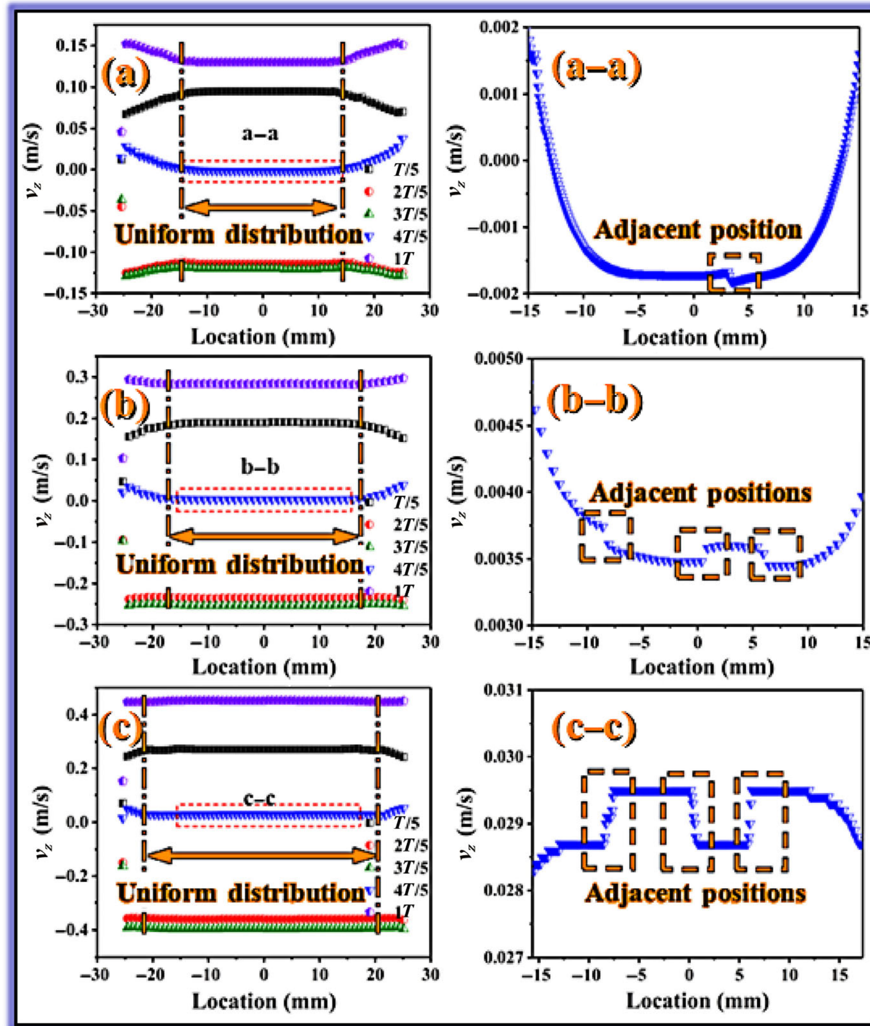

Fig. 7 Slurry v_z distribution curves under different amplitudes on the A–A line (Fig. 5): (a) 1 μm; (b) 2 μm; and (c) 3 μm.

4.1.2 *Pressure field and air volume fraction (AVF)*

Relative pressure contours of the slurry at different amplitudes are displayed in Fig. 8. The slurry pressure varies periodically with time. It implies that a larger amplitude facilitates the acquisition of higher pressures at the same moment. As the amplitudes increase (1, 2, and 3 μm), the relative pressures in the central region are −68,892, −37,659, and 11,870 Pa, respectively. The pressure at the edge of the wafer is much higher. As observed from Eqs. (31) and (33), the stronger pressure means that the abrasive will initiate more cracks after impacting on the wafer surface. This is beneficial to improving the MRR.

Cavitation is helpful to increase chemical reaction rate and MRR. The AVF characterizes the cavitation intensity. Figure 9 provides the AVF contours at different ultrasonic amplitudes. The AVF is obviously higher in the central area, and it is 20%, 37%, and 49% under 1, 2, and 3 μm amplitudes, respectively. Moreover, the maximum AVF (the red region in Fig. 9) is mainly in the center, which can improve the MRR in the center. It helps to balance the bigger MRR effects of higher polishing velocity (Fig. 5) and pressure (Fig. 8) on the sapphire edge, thus obtaining the flatter polished surface.

The above studies show that altering the ultrasonic amplitude leads to significant modifications in slurry physical fields including the velocity, pressure, and AVF. The bigger ultrasonic amplitude is capable of achieving a higher MRR and a smoother surface through an enhanced hydro-dynamic contact mode.

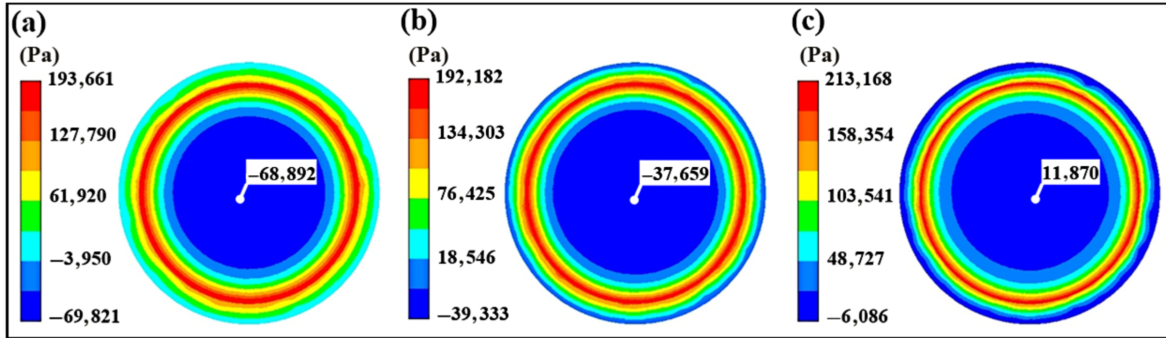

Fig. 8 Relative pressure contours of slurry at $3T/5$ at different amplitudes: (a) 1 μm; (b) 2 μm; and (c) 3 μm.

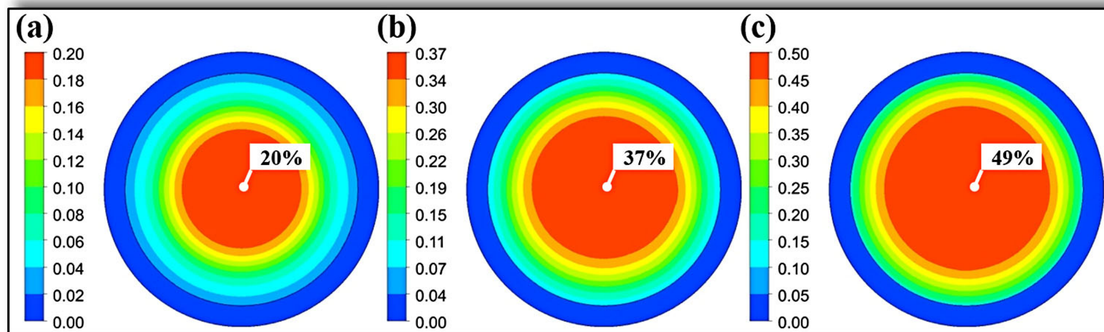

Fig. 9 AVF contours of slurry at $3T/5$ at different amplitudes: (a) 1 μm; (b) 2 μm; and (c) 3 μm.

This has been confirmed by Ref. [58] on ultrasonic amplitudes.

4.2 Effects of rotation speeds on slurry fields

4.2.1 Velocity field

Total velocity distribution curves of the slurry under different polishing speeds are shown in Fig. 10. The total velocity distribution is rotated at a speed of 40 r/min (Fig. 10(a)). The minimum and maximum velocities of the slurry at the center are 0.14 and 0.33 m/s in one cycle, respectively. The velocity variation is 0.19 m/s. The maximum velocity reaches 0.37 and 0.42 m/s under 60 and 80 r/min, respectively (Figs. 10(b) and 10(c), respectively). The velocity variations are reduced to 0.15 and 0.13 m/s, respectively. Furthermore, the higher the polishing speed is, the higher the average velocities of the slurry will be, as shown in Figs. 10(a)–10(c). Higher average velocities and lower velocity variations of the slurry can improve both the MRR and surface uniformity.

4.2.2 Pressure field and AVF

The curves of the average relative pressure in the slurry as a function of time are presented in Fig. 11. The curves of fluid pressures over time are highly overlapping at different speeds. This indicates that changes in rotational speeds hardly affect the slurry pressure. Again, it shows that it is the ultrasonic vibration that causes the periodic changes in the slurry pressure.

Figure 12 exhibits the AVF distribution curves of the fluid on the A–A line at different polishing speeds. In general, there is no perceptible effects of polishing speed variations on the AVF comparing Figs. 12(a)–12(c). This indicates that ultrasonic vibrations are also the main influences on the growth of AVF.

The CFD studies on rotational speeds have proven that changes in polishing speeds have effects on the slurry velocity field. The improvement in rotational speeds facilitates the increase in kinetic energy of abrasives and MRR. Nevertheless, its effects on the pressure and AVF are small. Material removal cannot be promoted by increasing l and cavitation with rising polishing speeds.

As far as hydro-dynamic contact mode is considered, the effects of ultrasonic amplitudes on the slurry

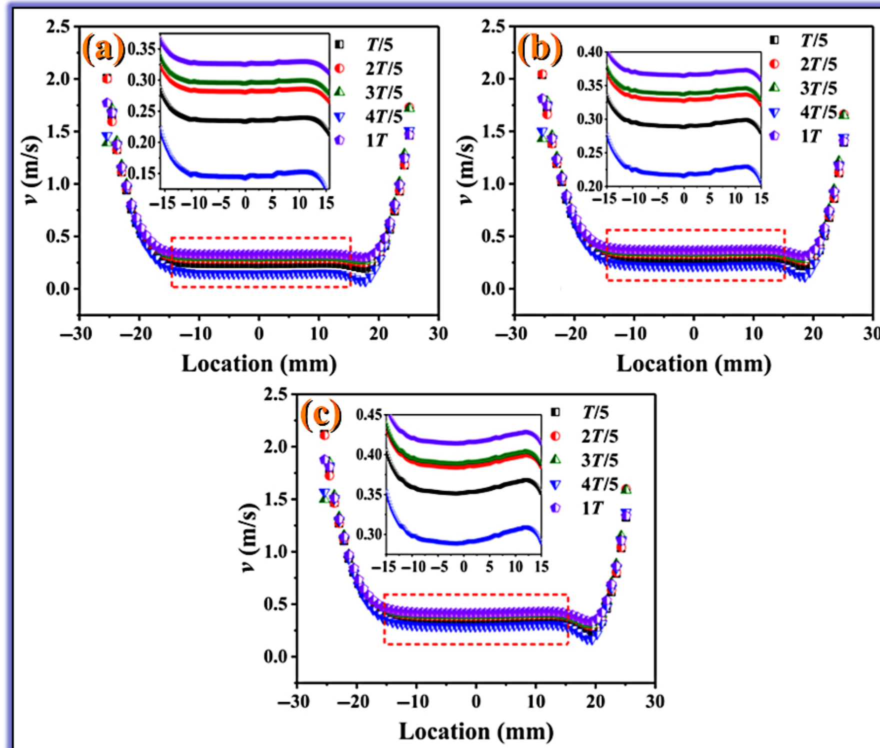

Fig. 10 Total velocity distribution curves of slurry on the A–A line (Fig. 5) under various rotating speeds: (a) 40 r/min; (b) 60 r/min; and (c) 80 r/min.

physical fields, including the velocity, pressure, and AVF, are stronger than those of the rotational speeds. In Section 5, sapphire polishing experiments were conducted to further explore the UA-CMP mechanism combining the AFM *in-situ* studies and CFD simulations.

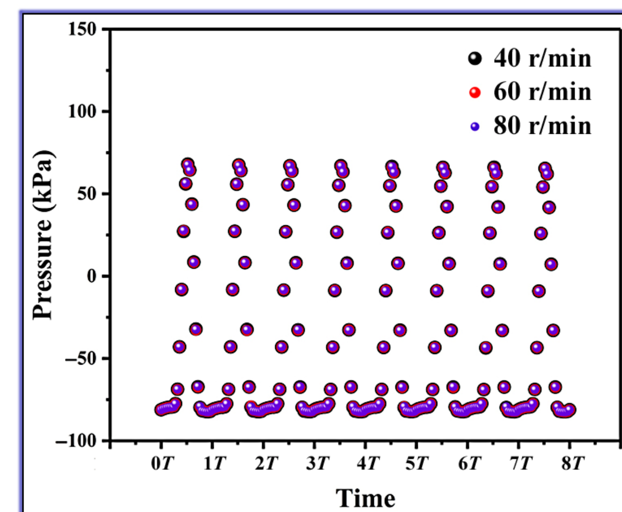

Fig. 11 Average relative pressure curves of slurry with time under various polishing speeds.

5 Sapphire UA-CMP experiments

The sapphire UA-CMP equipment was upgraded from a polisher (CMP Tribo, Bruker, USA) [58]. The experimental samples are two-inch *c*(0001) sapphire wafers. The 15% SiO_2 slurry was chosen for the experiments, and its diameter is about 60 nm (Fig. 1(b)). The material of the pad is damping fabric. The polishing speeds are 40, 60, and 80 r/min. The ultrasonic vibration frequency is 50 kHz, and the amplitude is 2 μm. They are consistent with the parameters in the CFD simulations. The polishing time and pressure are 1 h and 4 psi for each condition, respectively. The slurry flow rate is 80 mL/min. Sapphire was cleaned and dried after the procedure. The AFM was used to characterize the surface morphology and roughness after polishing. An electronic balance (0.01 mg) was applied to measure the sapphire mass. Then, MRR_{exp} (in μm/h) can be obtained by Eq. (39):

$$MRR_{exp} = \frac{10^4 \Delta M}{\rho S_n t_1} \quad (39)$$

where ΔM (in mg) is the loss of wafer mass, and t_1 is the polishing time (1 h).

In sapphire UA-CMP, one part of the removed material flows away with the slurry, while the other part may remain on the pad. In this paper, the pad surface composition is characterized by the energy dispersive spectroscopy (EDS; AZtec X-Max 80, Oxford Instruments, UK). It is confirmed that the material is indeed stripped from the sapphire surface in UA-CMP. Figures 13(a) and 13(b) present the SEM images and EDS energy spectra of the original pad (named pad (a)) and pad after polishing (named pad (b)), respectively. The EDS data show that the pad (a) does not contain Al element, but it exists in the pad (b). This indicates that the Al-containing compounds on the sapphire surface are adhered to the pad. The Al content is not high as a few materials are removed from the wafer surface. The highest Si content in the pad (b) suggests that a large amount of SiO_2 abrasives are imbedded in the pads. This provides a favorable

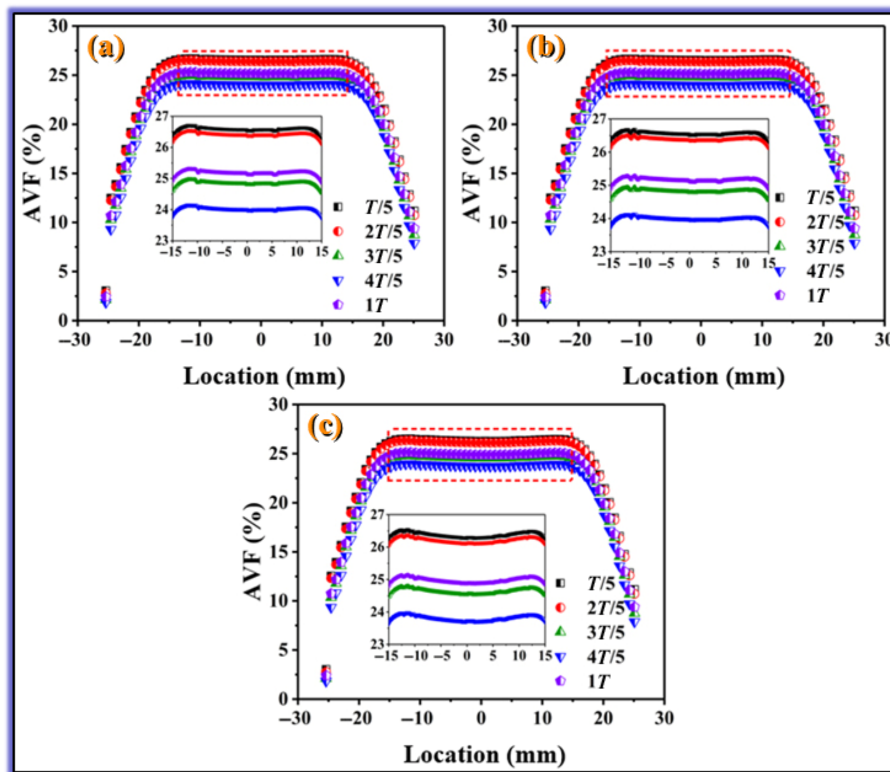

Fig. 12 AVF distribution curves of slurry on the A–A line (Fig. 5) under various polishing velocities: (a) 40 r/min; (b) 60 r/min; and (c) 80 r/min.

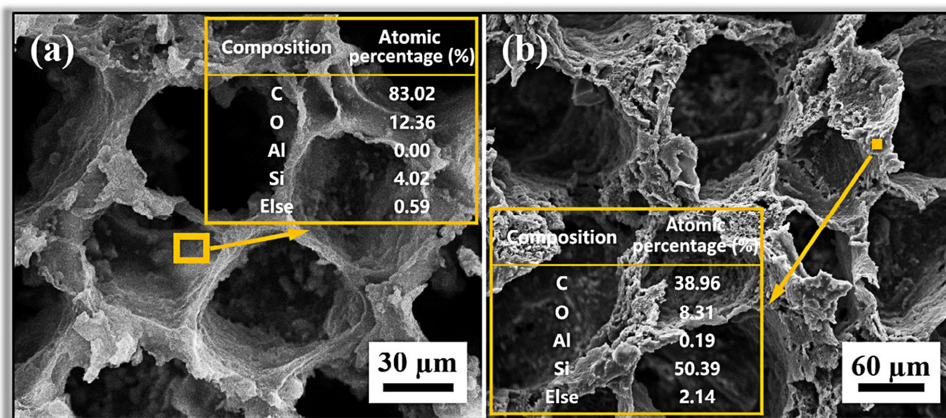

Fig. 13 SEM images and EDS results of polishing pad: (a) before polishing; (b) after UA-CMP.

evidence for the two-body wear. Further, there is only slight wear on the polishing pad surface in UA-CMP comparing Fig. 13(a) with Fig. 13(b). The pad (b) structure is intact and still able to transport slurry well.

Figure 14 displays the histograms of MRR at different polishing speeds. The MRR of sapphire UA-CMP is around 1.24 μm/h when the polishing speed is 40 r/min. As the speed increased to 60 and 80 r/min, the MRR was approximately 1.55 and 2.03 μm/h, respectively. The experimental results reveal that the rotating speed plays a vital role in the MRR. In the UA-CMP device, the pad's diameter is much bigger than that of the wafer. When the rotating speed increases, it means that the $v_{\mathrm{p-s}}$ also becomes larger. Combined with Eq. (28), $\mathrm{MRR_{TBW}}$ of two-body wear is proportional to $v_{\mathrm{p-s}}$. Thus the removed sapphire by two-body wear obviously rises. The CFD simulations indicate that rotating speeds have small influences on the material removal of hydro-dynamic contact mode. The ultrasonic vibration intensely changes the slurry fields/abrasives and thus to affect the sapphire MRR. In this way, higher rotating speeds can achieve greater MRRs by mainly influencing the solid–solid contact mode.

Figure 15 presents the AFM images of the sapphire surface morphology. Figure 15(a) is the original sapphire surface before polishing, and its R_{a} was around 31 nm. When the polishing speed is 40 r/min, the surface geometry of the polished sapphire is displayed in Fig. 15(b). The sapphire surface is not flat and has some pits, and its R_{a} is 0.10 nm. At 60 r/min, R_{a} drops to 0.08 nm, and the polished surface is flatter, but there is still visible surface damage, as shown in Fig. 15(c). At 80 r/min (Fig. 15(d)), the wafer surface quality is the best without pits and scratches, and its R_{a} is 0.07 nm.

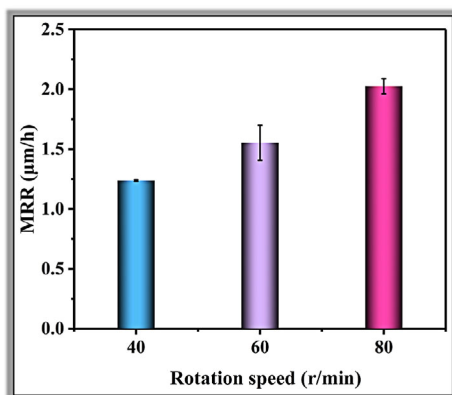

Fig. 14 Sapphire MRRs under various rotation speeds in UA-CMP.

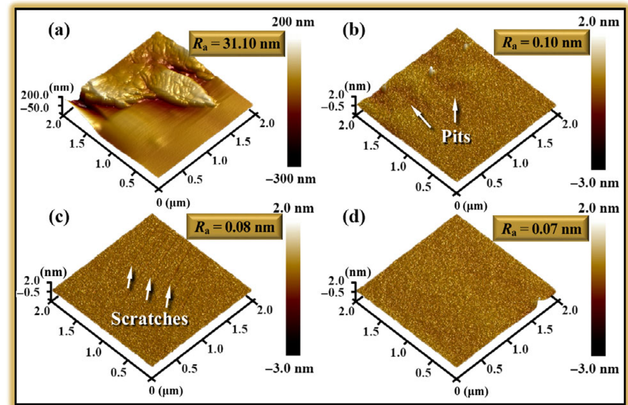

Fig. 15 AFM images of sapphire surface topography: (a) original sapphire surface; (b–d) after polishing at 40, 60, and 80 r/min.

The MRR is closely related to the surface quality in UA-CMP. For the same polishing time, the lower MRR means that the thickness of the removed material is thinner. Thus it is possible that smaller asperities on the wafer surface are not completely removed. It is also likely that there is residual surface damage, such as scratches, caused during the cutting of the sapphire. As the removed material thickness increases, the asperity and damage on the surface gradually disappear. Ultimately, a smoother and non-destructive sapphire surface is obtained [81].

6 Conclusions

The aim of this article is exploring the sapphire UA-CMP mechanism. Here, a material removal model was developed combining the solid–solid and hydro-dynamic contact modes. The feasibility of the two-body wear theory was verified by the AFM *in-situ* studies. The AFM tip was used to simulate an abrasive particle scribing on sapphire, achieve material removal, and observe the atomic step structure.

The CFD method visualized the effects of ultrasonic amplitudes and rotational speeds on the fluid flow behavior. These help to understand the influences of the process parameters on the hydro-dynamic contact mode during UA-CMP. Ultrasonic amplitudes have significant influences on the fluid fields. An enlarged amplitude is capable of apparently increasing the fluid flow velocity, pressure, and AVF. These enhancements of physical fields contribute to the MRR of the hydro-

dynamic contact mode. By contrast, the polishing speed variation has fewer effects on the hydro-dynamic contact pattern.

The sapphire UA-CMP experiments illustrate that higher rotational speeds achieve larger MRRs and better surface quality. The synthesis of experimental and simulation results implies that the rising rotational speed enables the efficient material removal mainly through two-body wear. From 40 to 80 r/min, the MRR increased around 63%. The surface roughness after polishing was reduced from 0.10 to 0.07 nm. The sapphire surface was smooth and undamaged.

Acknowledgements

This work was supported by the National Natural Science Foundation of China (Nos. 51865030 and 52165025).

Declaration of competing interest

The authors have no competing interests to declare that are relevant to the content of this article.

Open Access This article is licensed under a Creative Commons Attribution 4.0 International License, which permits use, sharing, adaptation, distribution and reproduction in any medium or format, as long as you give appropriate credit to the original author(s) and the source, provide a link to the Creative Commons licence, and indicate if changes were made.

The images or other third party material in this article are included in the article's Creative Commons licence, unless indicated otherwise in a credit line to the material. If material is not included in the article's Creative Commons licence and your intended use is not permitted by statutory regulation or exceeds the permitted use, you will need to obtain permission directly from the copyright holder.

To view a copy of this licence, visit http://creativecommons.org/licenses/by/4.0/.

References

[1] Bristow J K, Tiana D, Parker S C, Walsh A. Defect chemistry of Ti and Fe impurities and aggregates in Al_2O_3. *J Mater Chem A* **2**(17): 6198–6208 (2014)

[2] Khattak C P, Shetty R, Schwerdtfeger C R, Ullal S. World's largest sapphire for many applications. *J Cryst Growth* **452**: 44–48 (2016)

[3] Zhang B C, Lei H, Chen Y. Preparation of Ag_2O modified silica abrasives and their chemical mechanical polishing performances on sapphire. *Friction* **5**(4): 429–436 (2017)

[4] Xu L, Lei H. Nano-scale surface of ZrO_2 ceramics achieved efficiently by peanut-shaped and heart-shaped SiO_2 abrasives through chemical mechanical polishing. *Ceram Int* **46**(9): 13297–13306 (2020)

[5] Chen H, Guo D, Xie G X, Pan G S. Mechanical model of nanoparticles for material removal in chemical mechanical polishing process. *Friction* **4**(2): 153–164 (2016)

[6] Dong Y, Lei H, Chen Y, Liu W Q, Xu L, Wang T X, Dai S W. Preparation of irregular silica nanoparticles by the polymer templating for chemical mechanical polishing of sapphire substrates. *J Electron Mater* **48**(7): 4598–4606 (2019)

[7] Zhou Y, Pan G S, Shi X L, Gong H, Zou C L, Xu L. Effects of silica abrasive size on sapphire CMP performances and their removal mechanisms. In: Proceedings of the 2015 International Conference on Planarization/CMP Technology (ICPT), Chandler, USA, 2015: 1–3.

[8] Kwon T Y, Ramachandran M, Park J G. Scratch formation and its mechanism in chemical mechanical planarization (CMP). *Friction* **1**(4): 279–305 (2013)

[9] Zhao D W, Lu X C. Chemical mechanical polishing: Theory and experiment. *Friction* **1**(4): 306–326 (2013)

[10] Zhang Z Y, Liu J, Hu W, Zhang L Z, Xie W X, Liao L X. Chemical mechanical polishing for sapphire wafers using a developed slurry. *J Manuf Process* **62**: 762–771 (2021)

[11] Xie W X, Zhang Z Y, Liao L X, Liu J, Su H J, Wang S D, Guo D M. Green chemical mechanical polishing of sapphire wafers using a novel slurry. *Nanoscale* **12**(44): 22518–22526 (2020)

[12] Zhang Z Y, Cui J F, Zhang J B, Liu D D, Yu Z J, Guo D M. Environment friendly chemical mechanical polishing of copper. *Appl Surf Sci* **467–468**: 5–11 (2019)

[13] Zhang Z Y, Liao L X, Wang X Z, Xie W X, Guo D M. Development of a novel chemical mechanical polishing slurry and its polishing mechanisms on a nickel alloy. *Appl Surf Sci* **506**: 144670 (2020)

[14] Zhang Z Y, Shi Z F, Du Y F, Yu Z J, Guo L C, Guo D M. A novel approach of chemical mechanical polishing for a titanium alloy using an environment-friendly slurry. *Appl Surf Sci* **427**: 409–415 (2018)

[15] Xu L, Zou C L, Shi X L, Pan G S, Luo G H, Zhou Y. Fe–N_x/C assisted chemical–mechanical polishing for improving the removal rate of sapphire. *Appl Surf Sci* **343**: 115–120 (2015)

[16] Zhu H L, Tessaroto L A, Sabia R, Greenhut V A, Smith M, Niesz D E. Chemical mechanical polishing (CMP) anisotropy in sapphire. *Appl Surf Sci* **236**(1–4): 120–130 (2004)

[17] Wang X, Lei H, Chen R L. CMP behavior of alumina/metatitanic acid core–shell abrasives on sapphire substrates. *Precis Eng* **50**: 263–268 (2017)

[18] Dai S W, Lei H, Fu J F. Preparation of SiC/SiO_2 hard core–soft shell abrasive and its CMP behavior on sapphire substrate. *J Electron Mater* **49**(2): 1301–1307 (2020)

[19] Liu T T, Lei H. Nd^{3+}-doped colloidal SiO_2 composite abrasives: Synthesis and the effects on chemical mechanical polishing (CMP) performances of sapphire wafers. *Appl Surf Sci* **413**: 16–26 (2017)

[20] Wang T X, Lei H. Novel polyelectrolyte–Al_2O_3/SiO_2 composite nanoabrasives for improved chemical mechanical polishing (CMP) of sapphire. *J Mater Res* **34**(6): 1073–1082 (2019)

[21] Xu L, Zhang X, Kang C X, Wang R R, Zou C L, Zhou Y, Pan G S. Preparation of a novel catalyst ($SoFe^{III}$) and its catalytic performance towards the removal rate of sapphire substrate during CMP process. *Tribol Int* **120**: 99–104 (2018)

[22] Gao S, Kang R K, Jin Z J, Dong Z G. Research on the polishing performance of CMP slurry for the sapphire crystal. *Adv Mater Res* **325**: 457–463 (2011)

[23] Zhao X, Niu X H, Yin D, Wang J C, Zhang K. Research on *R*-plane sapphire substrate CMP removal rate based on a new-type alkaline slurry. *ECS J Solid State Sc* **7**(3): P135–P141 (2018)

[24] Li Z Y, Deng Z H, Hu Y X. Effects of polishing parameters on surface quality in sapphire double-sided CMP. *Ceram Int* **46**(9): 13356–13364 (2020)

[25] Zhang Z F, Yan W X, Zhang L, Liu W L, Song Z T. Effect of mechanical process parameters on friction behavior and material removal during sapphire chemical mechanical polishing. *Microelectron Eng* **88**(9): 3020–3023 (2011)

[26] Li Z Y, Deng Z H, Ge J M, Liu T, Wan L L. Experimental and theoretical analysis of single-sided and double-sided chemical mechanical polishing of sapphire wafers. *Int J Adv Manuf Tech* **119**(7): 5095–5106 (2022)

[27] Wang L, Zhou P, Yan Y, Kang R K, Guo D M. Physically-based modeling of pad–asperity scale chemical–mechanical synergy in chemical mechanical polishing. *Tribol Int* **138**: 307–315 (2019)

[28] Moriwaki T, Shamoto E. Ultraprecision diamond turning of stainless steel by applying ultrasonic vibration. *CIRP Ann* **40**(1): 559–562 (1991)

[29] Moriwaki T, Shamoto E, Inoue K. Ultraprecision ductile cutting of glass by applying ultrasonic vibration. *CIRP Ann* **41**(1): 141–144 (1992)

[30] Klocke F, Rübenach O. Ultrasonic assisted diamond turning of steel and glass. In: Proceedings of the International Seminar on Precision Engineering and Micro Technology, Aachen, Germany, 2000: 179–189.

[31] Moriwaki T, Shamoto E. Recent development in ultraprecision machining and machine tool technology. In: Proceedings of the Precision Engineering and Micro Technology Proceedings, Aachen, Germany, 2000: 19–20.

[32] Chen G, Ren C Z, Zou Y H, Qin X D, Lu L P, Li S P. Mechanism for material removal in ultrasonic vibration helical milling of Ti_6Al_4V alloy. *Int J Mach Tools Manu* **138**: 1–13 (2019)

[33] Agarwal S. On the mechanism and mechanics of material removal in ultrasonic machining. *Int J Mach Tools Manu* **96**: 1–14 (2015)

[34] Xu W H, Lu X C, Pan G S, Luo J B, Zhang C H. Experimental study of ultrasonic vibration assisted chemical mechanical polishing for sapphire substrate. In: *Advanced Tribology*. Luo J B, Meng Y G, Shao T M. Zhao Q, Eds. Berlin: Springer Berlin Heidelberg, 2009: 464–466.

[35] Wang H, Pei Z J, Cong W L. A feeding-directional cutting force model for end surface grinding of CFRP composites using rotary ultrasonic machining with elliptical ultrasonic vibration. *Int J Mach Tools Manu* **152**: 103540 (2020)

[36] Xu W H, Lu X C, Pan G S, Lei Y Z, Luo J B. Ultrasonic flexural vibration assisted chemical mechanical polishing for sapphire substrate. *Appl Surf Sci* **256**(12): 3936–3940 (2010)

[37] Xu W H, Lu X C, Pan G S, Lei Y Z, Luo J B. Effects of the ultrasonic flexural vibration on the interaction between the abrasive particles; pad and sapphire substrate during chemical mechanical polishing (CMP). *Appl Surf Sci* **257**(7): 2905–2911 (2011)

[38] Zhong M, Yuan R J, Li X B, Chen J F, Xu W H. Effects of abrasive particles and pads' characteristics on ultrasonic assisted chemical mechanical polishing for sapphire. *China Surf Eng* **31**(6): 125–132 (2018) (in Chinese)

[39] Deng H G, Zhong M, Xu W H. Effects of different dispersants on chemical reaction and material removal in ultrasonic assisted chemical mechanical polishing of sapphire. *ECS J Solid State Sc* **11**(3): 033007 (2022)

[40] Preston F W. The theory and design of plate glass polishing machines. *J Glass Tech* **11**(44): 214–256 (1927)

[41] Su Y T, Hung T C, Chang Y Y. On machining rate of hydrodynamic polishing process under semi-contact lubricating condition. *Wear* **220**(1): 22–33 (1998)

[42] Luo J F, Dornfeld D A. Material removal mechanism in chemical mechanical polishing: Theory and modeling. *IEEE T Semiconduct M* **14**(2): 112–133 (2001)

[43] Chen R L, Li S X. Novel three-body nano-abrasive wear mechanism. *Friction* **10**(5): 677–687 (2022)

[44] Chen R L, Jiang R R, Lei H, Liang M. Material removal mechanism during porous silica cluster impact on crystal silicon substrate studied by molecular dynamics simulation. *Appl Surf Sci* **264**: 148–156 (2013)

[45] Chen R L, Luo J B, Guo D, Lu X C. Extrusion formation mechanism on silicon surface under the silica cluster impact studied by molecular dynamics simulation. *J Appl Phys* **104**(10): 104907 (2008)

[46] Chen R L, Luo J B, Guo D, Lu X C. Surface damages on silicon surfaces created by large silica cluster impacts: Molecular dynamics simulation. In: *Advanced Tribology*. Luo J B, Meng Y G, Shao T M. Zhao Q, Eds. Berlin: Springer Berlin Heidelberg, 2009: 582–583.

[47] Chen R L, Luo J B, Guo D, Lei H. Dynamic phase transformation of crystalline silicon under the dry and wet impact studied by molecular dynamics simulation. *J Appl Phys* **108**(7): 073521 (2010)

[48] Zarepour H, Yeo S H. Single abrasive particle impingements as a benchmark to determine material removal modes in micro ultrasonic machining. *Wear* **288**: 1–8 (2012)

[49] Luo J F, Dornfeld D A. Material removal regions in chemical mechanical planarization for submicron integrated circuit fabrication: Coupling effects of slurry chemicals, abrasive size distribution, and wafer–pad contact area. *IEEE T Semiconduct M* **16**(1): 45–56 (2003)

[50] Chen R L, Li S X, Wang Z, Lu X C. Mechanical model of single abrasive during chemical mechanical polishing: Molecular dynamics simulation. *Tribol Int* **133**: 40–46 (2019)

[51] Cook L M. Chemical processes in glass polishing. *J Non-Cryst Solids* **120**(1–3): 152–171 (1990)

[52] Fu G H, Chandra A, Guha S, Subhash G. A plasticity-based model of material removal in chemical–mechanical polishing (CMP). *IEEE T Semiconduct M* **14**(4): 406–417 (2001)

[53] Zhou J N, Cao Z C, Zhang J P, Zhao C Y, Liu H T. Development and theoretical analysis of novel surface adaptive polishing process for high-efficiency polishing of optical freeform surface. *J Manuf Process* **80**: 874–886 (2022)

[54] Nguyen V T, Fang T H. Abrasive mechanisms and interfacial mechanics of amorphous silicon carbide thin films in chemical–mechanical planarization. *J Alloys Compd* **845**: 156100 (2020)

[55] Wang S, Zhao Q L, Yang X D. Surface and subsurface microscopic characteristics in sapphire ultra-precision grinding. *Tribol Int* **174**: 107710 (2022)

[56] Karimi A, Martin J L. Cavitation erosion of materials. *Int Mater Rev* **31**(1): 1–26 (1986)

[57] Liu D F, Yan R M, Chen T. Material removal model of ultrasonic elliptical vibration-assisted chemical mechanical polishing for hard and brittle materials. *Int J Adv Manuf Tech* **92**(1): 81–99 (2017)

[58] Zhou M F, Zhong M, Xu W H. Effects of ultrasonic amplitude on sapphire ultrasonic vibration assisted chemical mechanical polishing by experimental and CFD method. *Mech Adv Mater Struc* **29**: 7086–7103 (2022)

[59] Popov V L. *Contact Mechanics and Friction: Physical Principles and Applications*. Berlin: Springer Berlin Heidelberg, 2010.

[60] Yu T K, Yu C C, Orlowski M. A statistical polishing pad model for chemical–mechanical polishing. In: Proceedings of the IEEE International Electron Devices Meeting, Washington, USA, 1993: 865–868.

[61] Johnson K L. *Contact Mechanics*. Cambridge (UK): Cambridge University Press, 1987.

[62] Zhou Y, Pan G S, Shi X L, Gong H, Xu L, Zou C L. AFM and XPS studies on material removal mechanism of sapphire wafer during chemical mechanical polishing (CMP). *J Mater Sci-Mater El* **26**(12): 9921–9928 (2015)

[63] Shi X L, Pan G S, Zhou Y, Xu L, Zou C L, Gong H. A study of chemical products formed on sapphire (0001) during chemical–mechanical polishing. *Surf Coat Technol* **270**: 206–220 (2015)

[64] Zhou Y, Pan G S, Shi X L, Zhang S M, Gong H, Luo G H. Effects of ultra-smooth surface atomic step morphology on chemical mechanical polishing (CMP) performances of sapphire and SiC wafers. *Tribol Int* **87**: 145–150 (2015)

[65] Shi X L, Xu L, Zhou Y, Zou C L, Wang R R, Pan G S. An *in situ* study of chemical–mechanical polishing behaviours on sapphire (0001) via simulating the chemical product-removal process by AFM-tapping mode in both liquid and air environments. *Nanoscale* **10**(42): 19692–19700 (2018)

[66] Furumoto T, Saito R, Watanabe K, Ochi Y, Hashimoto Y, Yamaguchi M, Koyano T, Hosokawa A. Thermal stress cleavage of a single-crystal round sapphire bar by carbon dioxide laser. *J Mater Process Tech* **297**: 117237 (2021)

[67] Lin Z C, Huang W S, Tsai J S. A study of material removal amount of sapphire wafer in application of chemical mechanical polishing with different polishing pads. *J Mech Sci Technol* **26**(8): 2353–2364 (2012)

[68] Zhu H L, Niesz D E, Greenhut V A, Sabia R. The effect of abrasive hardness on the chemical-assisted polishing of (0001) plane sapphire. *J Mater Res* **20**(2): 504–520 (2005)

[69] Hou Z Y, Niu X H, Lu Y N, Zhang Y C, Zhu Y B. Effect of ZnO–SiO_2 composite abrasive on sapphire polishing performance and mechanism analysis. *ECS J Solid State Sc* **10**(10): 104001 (2021)

[70] Vijayakumar A, Du T, Sundaram K B, Desai V. Polishing mechanism of tantalum films by SiO_2 particles. *Microelectron Eng* **70**(1): 93–101 (2003)

[71] Zhao Y W, Chang L. A micro-contact and wear model for chemical–mechanical polishing of silicon wafers. *Wear* **252**(3–4): 220–226 (2002)

[72] Xu Y C, Lu J, Xu X P. Study on planarization machining of sapphire wafer with soft–hard mixed abrasive through mechanical chemical polishing. *Appl Surf Sci* **389**: 713–720 (2016)

[73] Wang Y G, Zhao Y W, Gu J. A new nonlinear-micro-contact model for single particle in the chemical–mechanical polishing with soft pad. *J Mater Process Tech* **183**(2–3): 374–379 (2007)

[74] Qin C J, Hu Z H, Tang A M, Yang Z P, Luo S. An efficient material removal rate prediction model for cemented carbide inserts chemical mechanical polishing. *Wear* **452–453**: 203293 (2020)

[75] Gruninger M F, Lawn B R, Farabaugh E N, Wachtman J B. Measurement of residual stresses in coatings on brittle substrati by indentation fracture. *J Am Ceram Soc* **70**(5): 344–348 (1987)

[76] Lawn B R, Evans A G, Marshall D B. Elastic/plastic indentation damage in ceramics: The median/radial crack system. *J Am Ceram Soc* **63**(9–10): 574–581 (1980)

[77] Liang Y D, Chen X, Niu J K, Zhang C, Ma Z L, Xu P F, Li M, Yu T B, Zhao J. Predictive and experimental research on the polishing slurry consumption model for ultrasonic vibration-assisted polishing of optical glass BK7. *Ceram Int* **48**(7): 10048–10058 (2022)

[78] Shi X L, Pan G S, Zhou Y, Gu Z H, Gong H, Zou C L. Characterization of colloidal silica abrasives with different sizes and their chemical–mechanical polishing performance on 4H-SiC(0001). *Appl Surf Sci* **307**: 414–427 (2014)

[79] Kumar A, Kovalchenko A, Pogue V, Pashchenko E, Melkote S N. Ductile mode behavior of silicon during scribing by spherical abrasive particles. *Procedia CIRP* **45**: 147–150 (2016)

[80] Sheng C, Zhong M, Xu W H. A study on mechanism of sapphire polishing using the diamond abrasive by molecular dynamics. *Mech Adv Mater Struc* **30**: 319–331 (2023)

[81] Wang R R, Guo D, Xie G X, Pan G S. Atomic step formation on sapphire surface in ultra-precision manufacturing. *Sci Rep* **6**(1): 29964 (2016)

Mufang ZHOU. He received his bachelor degree in mechanical engineering in 2019 from Hebei University of Engineering, China, and his master degree in mechanical engineering in 2022 from Nanchang University, China. Now he is a Ph.D. student in Key Laboratory of Tribology, Nanchang University, China. His research interest is ultrasonic vibration–chemical mechanical polishing for sapphire.

Wenhu XU. He received his Ph.D. degree in mechanical engineering from Tsinghua University, China, in 2011. From 2011 to 2016, he worked at China National Offshore Oil Corporation (CNOOC) Research Institute Ltd., China, as a mechanical engineer. Since 2016, he has worked at Nanchang University, China, and his current position is a professor. His research areas cover chemical mechanical polishing, friction material, and food oral tribology.